A Real-Time Online Data Product that Automatically Detects Easterly Gap-Flow Events and Precipitation Type in the Columbia River Gorge

PAUL J. NEIMAN, DANIEL J. GOTTAS, AND ALLEN B. WHITE

NOAA/Earth System Research Laboratory/Physical Sciences Division, Boulder, Colorado

WILLIAM R. SCHNEIDER AND DAVID R. BRIGHT

NOAA/National Weather Service Forecast Office, Portland, Oregon

(Manuscript received 6 June 2018, in final form 7 August 2018)

ABSTRACT

A real-time, hourly updated, online graphical data product that displays the depth and strength of easterly gap flow in the Columbia River Gorge using a 915-MHz Doppler wind profiler is presented. During precipitation events, this data product also displays observed precipitation accumulation and diagnosed precipitation type using measurements provided by a collocated heated tipping-bucket rain gauge, an optical disdrometer, and temperature and relative humidity sensors. Automated algorithms that determine the existence and depth of the gap flow, as well as precipitation type, are described. The Columbia River Gorge is the only major gap in the Cascade Mountains of Oregon and Washington. Consequently, both easterly and westerly directed gap-flow events are common in this region. Especially during late autumn and winter, easterly gap flow can cause hazardous and damaging weather (e.g., snow, freezing rain, and strong winds) in the Portland, Oregon–Vancouver, Washington metropolitan area. The product described here was developed to help forecasters at the Portland National Weather Service Forecast Office monitor cool-season easterly gap-flow events in order to provide situational awareness and guide warnings to the public about potential weather-related hazards.

1. Introduction

The channeling of air through breaches in mountainous terrain is referred to as gap flow. To first order, gap flows occur in response to a gap-parallel pressure gradient (Colman and Dierking 1992) and is sustained when that pressure gradient force is balanced by inertial forces (Glickman 2000). Gap flows can act as a source of cold air in temperate coastal regions including the west coast of North America (e.g., Overland and Walter 1981; Bond et al. 1997; Loescher et al. 2006; Colle et al. 2006, Neiman et al. 2006) and can locally lower snow levels in these regions relative to what the large-scale maritime conditions would dictate (Steenburgh et al. 1997). A prominent and recurring example of shallow gap flow occurs in the Pacific Northwest through the Columbia River Gorge (Fig. 1; see also Sharp and Mass 2002, 2004). The width of the gorge is generally 6–12 km below ~600 m MSL and widens to ~80 km in the layer between 600 and 2000 m MSL. During the warm season, high pressure dominates offshore and low pressure dominates inland. This results in a downgradient westerly gap flow of cool maritime air into the warm interior. The opposite scenario occurs frequently in winter, resulting in the westward extrusion (i.e., easterly gap flow) of cold continental air to the populous metropolitan area of Portland, Oregon, and Vancouver, Washington. Consequently, the Columbia River Gorge region is home to dozens of wind-farm networks because of the reliable wind resource provided by gap flows in both directions. The real-time observation-based data product described below focuses on the offshore-directed gap flows because of their potential hazardous impacts across the populous Portland metropolitan area. In contrast, inland-directed gap flows pose far fewer hazards there and are therefore not addressed.

The Columbia Gorge is the only major low-elevation (i.e., near sea level) gap in the Cascade Mountains of Oregon and Washington, and therefore is the focus for gap-flow events in this region. The Cascades separate the normally moist maritime climate to the west from

Corresponding author: Paul J. Neiman, paul.j.neiman@noaa.gov

DOI: 10.1175/JTECH-D-18-0088.1

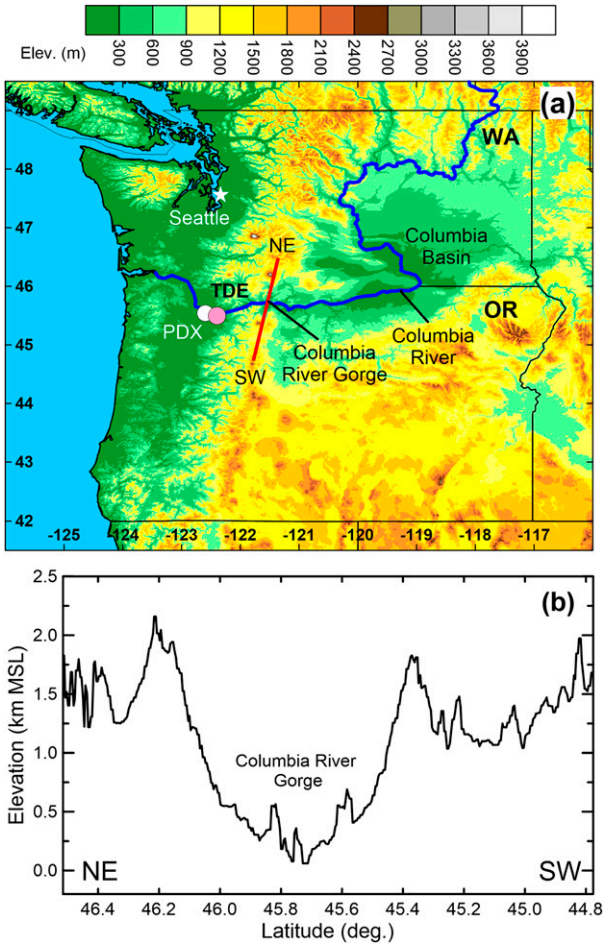

FIG. 1. (a) Terrain base map (m) of Oregon (OR) and Washington (WA), showing the locations of the observing site at Troutdale Airport (TDE; pink dot), Portland International Airport (PDX; white dot, located in the southeastern portion of the Portland–Vancouver Metropolitan area), Seattle (white star), and the Columbia River (marked in blue). (b) Terrain cross section across the Columbia River Gorge [see red NE–SW line in (a)].

the predominantly drier continental climate to the east. During the cool season, easterly gap-flow events are capable of producing damaging winds not necessarily accompanied by precipitation in both the western Columbia River Gorge and around the Portland–Vancouver metropolitan area. Other times cold easterly gap flow undercuts moist onshore flow associated with an approaching low pressure trough or landfalling extratropical cyclone from the Pacific and induces intense wind and winter-type precipitation (i.e., snow and especially freezing rain). For example, Sharp and Mass (2002, 2004) showed that 90% of all freezing rain events recorded in Portland between 1984 and 1999 were associated with easterly to southeasterly wind measured near the surface at Portland International Airport (PDX). Snowfall events during this period also occurred with primarily easterly to southeasterly flow, and snowfall amounts and frequency of freezing rain events increased when the strength of that flow increased. More generally during the winter at PDX, the easterly-to-southeasterly gap-flow wind sector accounts for a majority of all sectors.

To adequately warn the public about the impacts of easterly gap-flow events, forecasters need to know when gap flow is occurring, the speed and depth of the gap flow, the snow level, and the type and intensity of precipitation. Snow and freezing rain present particular hazards to the Portland–Vancouver region and to the challenge of forecasting low-level winter-type precipitation in this area. It has long been noted by forecasters at NOAA's Portland National Weather Service (NWS) Weather Forecast Office (WFO) that the suite of numerical weather prediction models in use often struggles to indicate the strength, depth, and duration of gap flows associated with the cold air intrusions. The NWS is increasingly striving to provide enhanced decision support services to core partners, such as emergency managers and other public officials to lessen the impacts of winter weather and wind storms in the region. Because of these forecast challenges and to improve the situational awareness of forecasters to help guide their warnings to the public, scientists at the Physical Sciences Division (PSD) of National Oceanic and Atmospheric Administration's Earth System Research Laboratory (NOAA/ESRL) have developed an observationally based gap-flow detection and precipitation typing data product. This product was initially presented to leadership in NOAA's NWS Portland WFO and is now described here.

Section 2 describes the relevant observing systems and their geographic locations. The real-time online data product is presented in section 3. The autodetection methodologies used to identify gap flows and precipitation types are described in detail in section 4. Concluding thoughts are offered in section 5.

2. Observing systems

A network of instruments was deployed in the Columbia River Gorge and Columbia basin of eastern Oregon and Washington in the autumn of 2015 for the second Wind Forecast Improvement Project (WFIP2), a public–private partnership funded by the U.S. Department of Energy (DOE) and NOAA. The primary goal of this 18-month campaign was to improve NWP model forecast skill for wind energy, with a focus on boundary layer parameterization used in numerical weather prediction and applied over complex terrain. At the western end of the gorge, the Troutdale, Oregon, Airport (TDE;

located at 12 m MSL and 15 km east-southeast of PDX; Fig. 1)—ideally situated to monitor offshore-directed gap glows—harbored a suite of observing systems that remain as a legacy from the project. Those instruments that provided data for the online data product are now described.

A 915-MHz radar wind profiler (Carter et al. 1995) provided hourly averaged profiles of horizontal wind in two modes, the lower of which is used in this study (i.e., radar range gates spanning from 0.15 to 2.52 km MSL with 58-m vertical resolution). Erroneous signals in the radar Doppler spectrum, arising from ground clutter contamination associated with moving trees, were identified and excluded from the spectral-peak-picking process. Then, the resulting spectral moments and derived wind data were edited objectively using the vertical–temporal continuity method of Weber et al. (1993). The combination of fine vertical resolution and continuous spatiotemporal coverage of high-quality winds is necessary to accurately depict the wind shear field, which is central to the gap-flow detection logic.

The spectral moments from the radar wind profiler's vertical beam were sampled using 60- and 105-m-resolution modes every ~3 min for precipitation detection and identification. Subhourly signal-to-noise-ratio and radial-velocity measurements were used to objectively detect the existence of a radar bright band (White et al. 2002), the height in the atmosphere at which falling snow transforms into rain (i.e., the snow level; White et al. 2010), and produce an hourly averaged snow level. The height difference between the snow level and the 0°C freezing level is ~200 m, on average, but can vary between ~120 and ~430 m depending on geographical location, lapse rate, snowfall rate, and sublimation (Stewart et al. 1984; White et al. 2010). The vertical proximity of the snow level to gap flows and to the ground surface influences the precipitation type observed at the surface, depending on the temperature. Thus, the same signal-to-noise-ratio and radial-velocity measurements were also used to aid in the automated precipitation-type identification near the surface.

A radio acoustic sounding system (RASS; Martner et al. 1993) provided hourly vertical profiles of virtual temperature from 0.15 to 1.59 km MSL at 60-m intervals, although strong winds associated with gap flows often reduce the vertical coverage to within a couple hundred meters above the radar. These were transformed into profiles of virtual potential temperature θ_v using surface pressure as a lower boundary and assuming a standard atmospheric pressure profile aloft. A 10-m tower collected surface observations every 2 min of pressure, temperature T, and relative humidity (from which wet-bulb temperature T_w was calculated) at 2 m above ground level (AGL) and wind velocity from a propeller-vane anemometer at 10 m AGL. A collocated heated tipping-bucket precipitation gauge gathered 2-min data. An OTT Particle Size and Velocity (PARSIVEL) disdrometer (Löffler-Mang and Joss 2000) measured the spectrum of hydrometeors sizes and fall velocities ($>0\,\mathrm{m\,s^{-1}}$ for downward) through its laser path, and these data were binned into 2-min blocks. The range of size and velocity measurements are 0.062–24.5 mm and $0.05–20.8\,\mathrm{m\,s^{-1}}$, respectively.

3. Real-time online data product

In this section we offer an example of the real-time online data product (Fig. 2). This example will also serve to provide meteorological and graphical context for the description of the product's automated methodologies presented in section 4. Figure 2 spans a 48-h period, and the associated display is updated hourly. Time increases from right to left to portray the advection of transient synoptic features from west to east. The observations are presented using dynamic color table ranges to fully highlight meteorological contrasts, except in Fig. 2b where the radar reflectivity color-table range is fixed.

The top two panels (Figs. 2a,b) are time–height sections of wind profiler data extending up to ~2.5 km MSL. Figure 2a contains hourly wind profiles color coded by speed. It can be used to identify transient flows (e.g., fronts, jets, ridge and trough axes) and shallow terrain-modulated winds (e.g., gap flows). The second time–height section (Fig. 2b) shows ~3-min-resolution radar reflectivity profiles from the vertical beam, calibrated using signal-to-noise ratio and surface disdrometer data (as in Williams et al. 2005). It provides spatiotemporal and intensity characteristics of precipitation,[1] and, when cast in dBZ units, allows for direct comparison with reflectivity values measured by operational scanning radars. The RASS time–height section (Fig. 2c) displays hourly profiles of wind and θ_v, the latter field highlighting thermodynamic stratification that helps distinguish differing air masses and the inversion depth if present. The height range is half that shown in Figs. 2a,b in order to highlight the full detail within the shallow RASS coverage. All three time–height sections, which are based on remote sensing observations, denote the snow level during precipitation when a radar bright band is present and mark the top of easterly gap-flow events

[1] The two horizontal layers of enhanced dBZ observed below 600 m MSL during times without precipitation are associated with ground clutter, as described in section 2. The same pattern of ground clutter is observed in Fig. 4b.

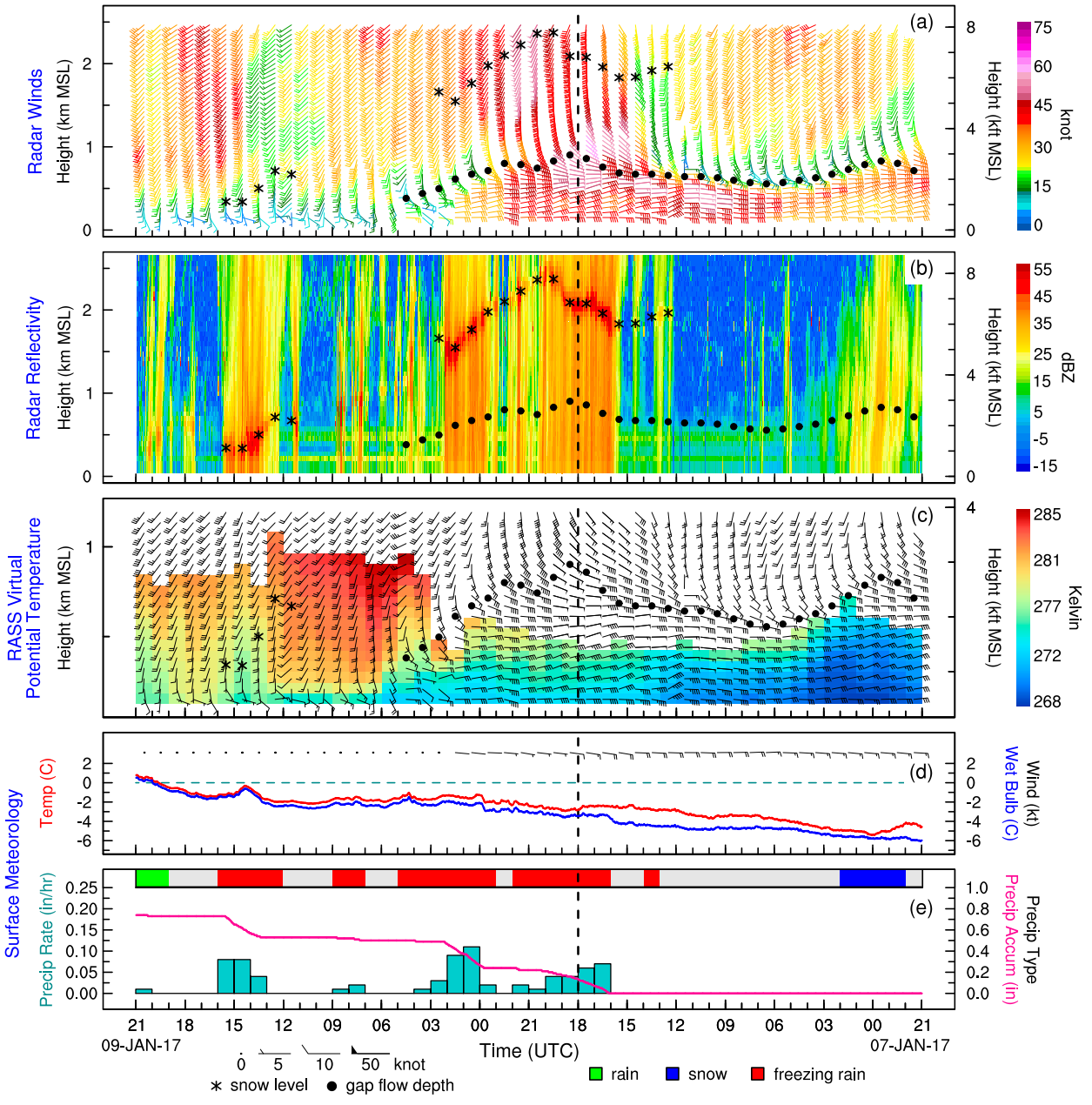

FIG. 2. An example of the real-time online data product at TDE between 2100 UTC 7 Jan and 2100 UTC 9 Jan 2017. (a) Time–height section of hourly radar wind profiles (flag: 50 kt, barb: 10 kt, half-barb: 5 kt) color coded by wind speed (kt). Hourly measurements of the snow level and the top of the gap flow are marked with stars and solid black dots, respectively. (b) Time–height section of ~3-min-resolution color-coded radar reflectivity (dBZ) from the vertical beam. The snow level and gap-flow top are marked as in (a). (c) Time–height section of hourly radar wind profiles [flags and barbs are as in (a)] and hourly color-coded RASS virtual potential temperature (K). The snow level and gap-flow top are marked as in (a). (d) Surface time series of hourly wind velocities [flags and barbs are as in (a); black dots portray observed wind speeds = 0], and 2-min-resolution temperature (red; °C) and wet-bulb temperature (blue; °C). The horizontal dashed green line marks 0°C, when present. (e) Color-coded hourly precipitation type (top of panel; color key at bottom), tipping-bucket hourly precipitation rate (in. h^{-1}; blue bars), and 2-min-resolution precipitation accumulation (in.; pink curve). The vertical black dashed line at 1800 UTC 8 Jan 2017 marks the time of the synoptic analyses in Fig. 3.

(derived via the automated methodology described in section 4a) on an hourly basis.

The bottom two panels (Figs. 2d,e) show time series of surface data collected from in situ instruments. In Fig. 2d, time series of 2-min temperature and wet-bulb temperature are displayed, as are hourly wind velocities. Figure 2e is devoted to precipitation, namely hourly precipitation rate, 2-min-resolution

precipitation accumulation, and the dominant hourly precipitation type of either rain, freezing rain, or snow (derived via the automated methodology described in section 4b). Because this online product is designed for the operational community in the United States, precipitation is expressed in English units (i.e., inches; 1 in. = 2.54 cm), as is wind speed (i.e., knots; 1 kt = 0.51 m s^{-1}).

The example shown in Fig. 2 spans the time period between 2100 UTC 7 January and 2100 UTC 9 January 2017. At near the midpoint of this period (i.e., at 1800 UTC 8 January 2017), a synoptic characterization is provided at 700, 850, and 1000 hPa (Fig. 3) using NOAA's Global Forecast System (GFS) forecast initialization at 0.5° × 0.5° horizontal resolution. A strong cyclone is situated over the Pacific offshore of Washington and Oregon, while a ridge dominates Southern California and the interior Intermountain West. Between these two features, a prominent down-height-gradient environment aligns with the Columbia River Gorge from the interior to the coast. Cold air is pooled in eastern Washington and Oregon's Columbia basin between 1000 and 850 hPa (i.e., between sea level and ~1.4 km MSL; Figs. 3b,c), while at 700 hPa (i.e., ~2.9 km MSL; Fig. 3a) the cyclone's warm sector covers the entirety of both states. Offshore, southwesterly flow is directed toward the coast ahead of an advancing polar cold front.

Figure 2 portrays strong 30–50-kt easterly gap flow within a cold stably stratified airstream confined to the lowest 0.5–1.0 km MSL. After 1800 UTC 8 January, the top of the gap flow temporally descends and then terminates at 0500 UTC 9 January. Concurrently, RASS θ_v shows shallowing cold gap flow being replaced with warmer southerly component maritime air. Aloft, southerly component flow dominates, and it is characterized by a temporal shift from moderate southwesterlies prior to 1400 UTC 8 January to strong southerlies centered at 2100 UTC 8 January to moderate southwesterlies thereafter. During the first 5 h of the 48-h period enhanced radar reflectivities lacking a bright band are observed, when strengthening southwesterlies aloft temporally descend with the approach of a warm front. The period between 1600 UTC 8 January and 0200 UTC 9 January is characterized by deep reflectivities and a bright band. The altitude of the bright band increases from 1.7 to 2.3 km MSL in strengthening southerlies associated with the warm sector of the oceanic extratropical cyclone, and then it descends to ~1.5 km MSL by 0200 UTC 9 January in weakening southwesterlies with the passage of the polar cold front aloft. Thereafter, temporally intermittent showery reflectivities and much lower brightband heights of <1 km MSL coincide with a post-cold-frontal air mass, although southwesterly flow persists aloft because the cyclone center remains offshore (not shown). Companion traces of surface T and T_w show cold but moderating continental conditions below freezing for the duration, eventually surpassing 0°C shortly before the end of the time series. Easterly surface winds until 0200 UTC 9 January highlight the gap flow, although observations of calm wind thereafter

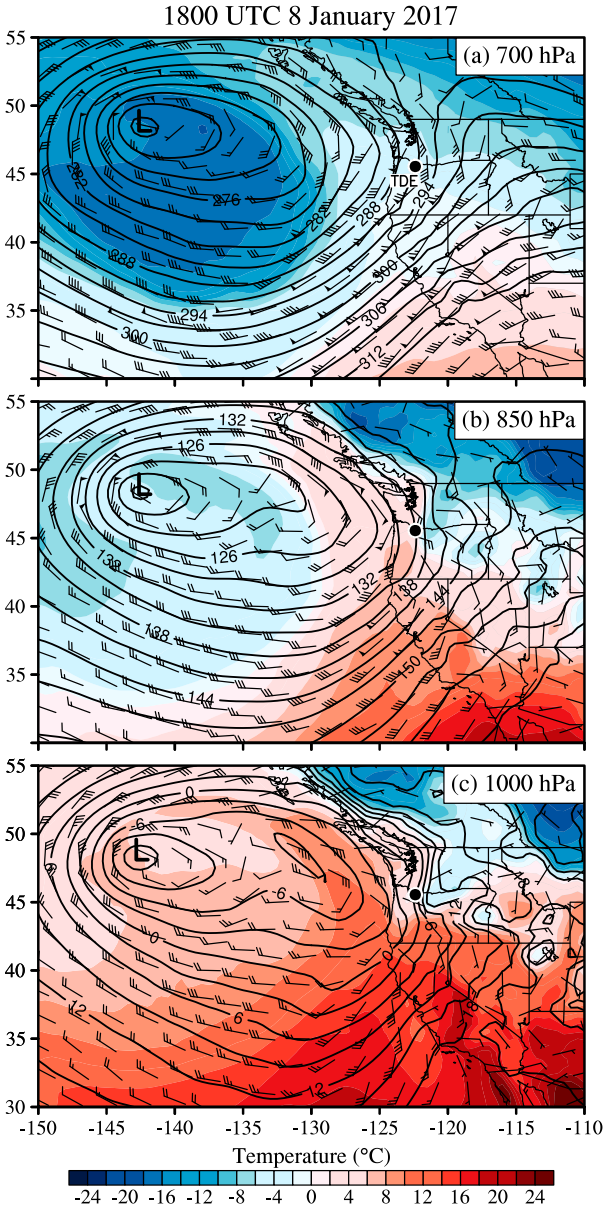

FIG. 3. Synoptic plan-view analyses of geopotential height (dam; black contours), temperature (°C; color fill), and wind velocities (flags and barbs are as in Fig. 1) at 1800 UTC 8 Jan 2017 using NOAA's GFS 0.5°-resolution initialization: (a) 700, (b) 850, and (c) 1000 hPa. In each panel, the cyclone center is marked with an "L" and the location of TDE is shown (black dot).

might actually indicate a temporary malfunction of the anemometer because of buildup of freezing rain (described below).

During the initial period of enhanced reflectivities ending at 0200 UTC 8 January (i.e., ahead of the advancing warm front) snow is diagnosed at the surface, although it is not measured by the tipping-bucket gauge perhaps because of catchment issues in the windy gap flow. Accumulating precipitation is recorded starting at 1600 UTC 8 January, totaling ~0.8 in. by the end of the period. Because a bright band is observed during this period, rain is falling. However, because of the presence of the shallow cold gap flow, the rain is falling into a subfreezing layer and is categorized as freezing rain when impacting a subfreezing surface. Only near the end of the 48-h period does T surpass the freezing mark, at which point the precipitation is marked as rain.

On occasion, synoptic-scale easterly component flow aloft occurs well above the Columbia River Gorge. During such episodes, it can be challenging to distinguish between the large-scale easterlies and the top of shallow terrain-induced gap flow in the gorge. Figure 4 highlights one such scenario on 5–7 December 2017. During this 48-h period, shallow and stably stratified easterly gap flow persists below ~1 km MSL in dry conditions. Aloft, prominent and deep easterly component flow is observed until ~0600 UTC 7 December, although an increasingly well-defined vertical directional shear from easterly to southeasterly is captured across the top of the autodetected gap flow after ~1200 UTC 6 December. After 1000 UTC 7 December weak winds aloft cap the unambiguous gap-flow regime, and this configuration persists for an additional week (not shown).

Synoptic analyses corresponding to the time of the deepest easterly flow observed at TDE at 0600 UTC 6 December are shown in Fig. 5. At 700 hPa (Fig. 5a), a strong, warm anticyclone is centered west of Seattle, Washington, at ~3.2 km MSL, with synoptic northeasterly flow occurring over TDE. At 850 hPa (i.e., ~1.6 km MSL; Fig. 5b), the strong and warm anticyclone is centered northwest of Seattle, with synoptic easterlies over TDE and cold continental air across eastern Oregon and Washington. The ridge aloft (i.e., at 700–850 hPa) migrates southeastward over TDE ~30 h later (not shown), resulting in the weak flow aloft observed at TDE. This general pattern persists for another week (not shown). Close to the surface at 1000 hPa (i.e., ~0.3 km MSL; Fig. 5c), a cold continental anticyclone is centered over southern Idaho and extends northwestward across the interior Pacific Northwest. Unlike aloft, the shallow easterly flow observed at TDE is terrain-induced rather than synoptic in scale. The cold low-level anticyclone persists in the interior for another week and sustains the shallow gap flow for the duration.

4. Autodetection methodologies for the online data product

a. *Gap-flow detection*

The automated identification of easterly gap-flow events hinges on key underlying physical characteristics of those events. As depicted in Fig. 6a, temporally persistent easterlies below ~1 km MSL define the gap flow for the 48-h period shown, with directional shear aloft starting after ~0600 UTC 6 December 2017. Within the gap flow, there are spatiotemporal jet-like patterns in the zonal component of the flow (u comp; Fig. 6b) and a lack of jet patterns in the meridional component (v comp; Fig. 6c). The autodetection methodology focuses on identifying the u-comp jet signatures and the associated flanking vertical shear in both the u comp and v comp. The magnitude of this shear term, along with its vertical gradient, will be used to determine the top of the gap flow (i.e., gap-flow depth) on an hourly basis. Here, we assume that a prominent vertical wind shear signature exists in the stably stratified transition atop the shallow continental air mass flowing unidirectionally westward through the Columbia Gorge, as was unambiguously documented for gap flows exiting California's Petaluma gap (Neiman et al. 2006).

The autodetection methodology begins by assessing the existence of gap flow on an hourly wind-profile basis. Gap flow in the Columbia River Gorge is considered present in each wind profile when the wind direction near the surface ranges between 50° and 120°, the low-level wind direction in the 0.1–0.35 km MSL layer ranges between 60° and 130° (rotated clockwise by 10° from the wind-direction range used near the surface to account for frictional effects), and the low-level u comp is ≤ -6.5 kt (≤ -3.35 m s^{-1}), similar to the criteria used for defining gap flows in the Petaluma study (Neiman et al. 2006). Based on a qualitative assessment of all gap-flow events observed over a 2-yr period at TDE (92 total), these directionality thresholds are equally applicable in both geographical locations. This assessment also revealed that the optimal threshold for the low-level u comp in the Columbia Gorge is 1.65 m s^{-1} weaker than the threshold used in the Petaluma study.

The wind velocities used in the gap-flow criteria are subjected to additional processing and substitutions to further accommodate the unique radar sampling and meteorological conditions at TDE. The low-level wind velocity is vertically averaged using four range gates between 0.1 and 0.35 km MSL for each hour, where this height range follows Neiman et al. (2006) but an additional radar gate is utilized in the fine-vertical-resolution mode at TDE. In addition, in contrast to Neiman et al. (2006), we substitute the wind velocity in

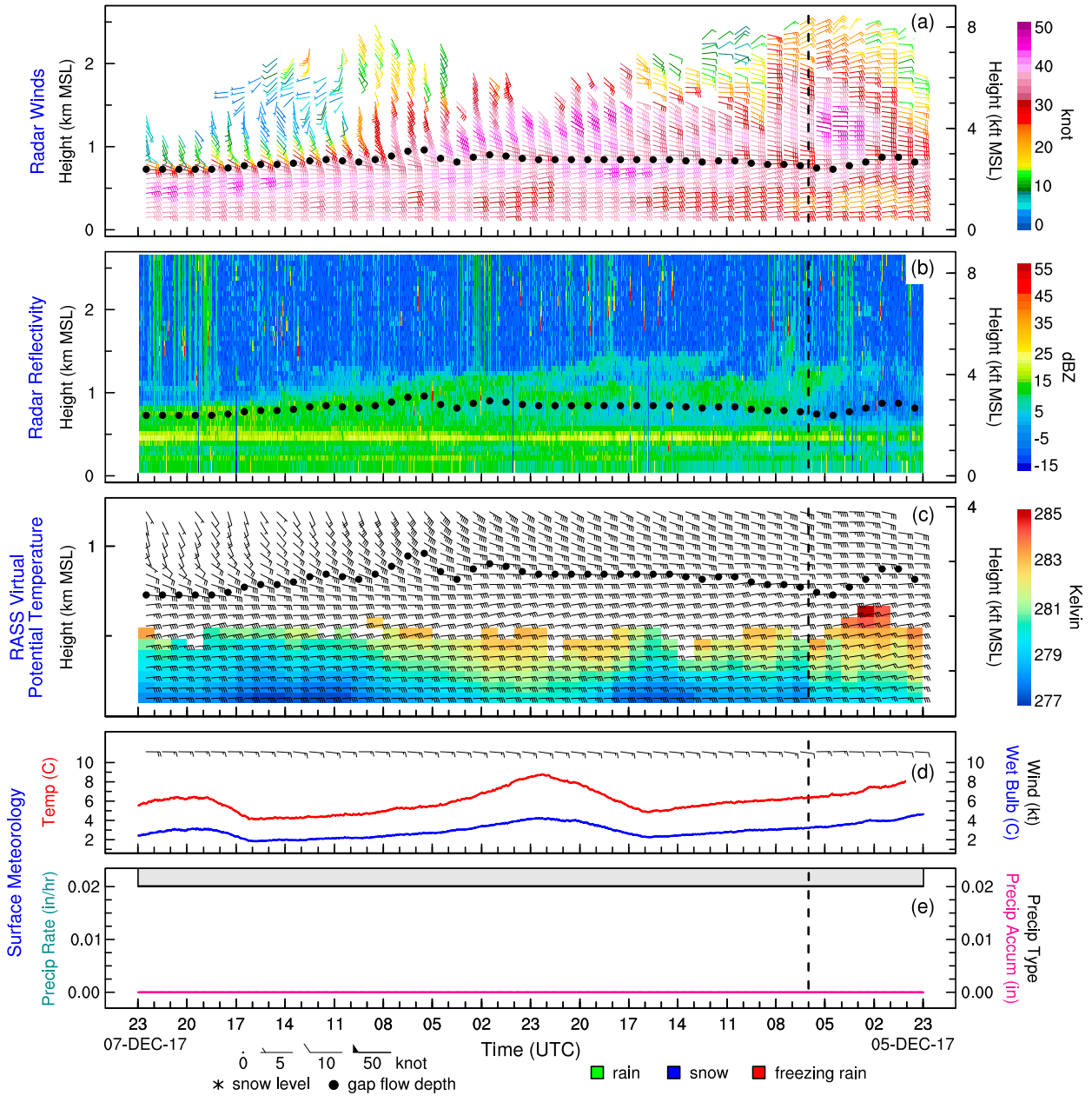

FIG. 4. As in Fig. 2, but for the time period between 2300 UTC 5 Dec and 2300 UTC 7 Dec 2017. The vertical black dashed line at 0600 UTC 6 Dec 2017 marks the time of the synoptic analyses in Fig. 5.

the lowest range gate (i.e., at 0.15 km MSL) for the surface wind because the surface flow at TDE can decouple from the gap flow immediately above the surface at the start and end of gap-flow events. If gap flow is present for a given hour in accordance with the aforementioned criteria, we continue with the ensuing five-step gap-flow autodetection logic.

The first step in that logic identifies all of the u-comp minima (i.e., the strongest easterly jets) in each vertical profile. It is assumed that the gap flow will correspond to one of these minima, as chosen at a later step in the algorithm. Initially, the u-comp time–height section in Fig. 6b is smoothed using a nine-point filter[2] to reduce

[2] See the description for the "smth9" function in the National Center for Atmospheric Research (NCAR) Command Language online user guide (https://www.ncl.ucar.edu/).

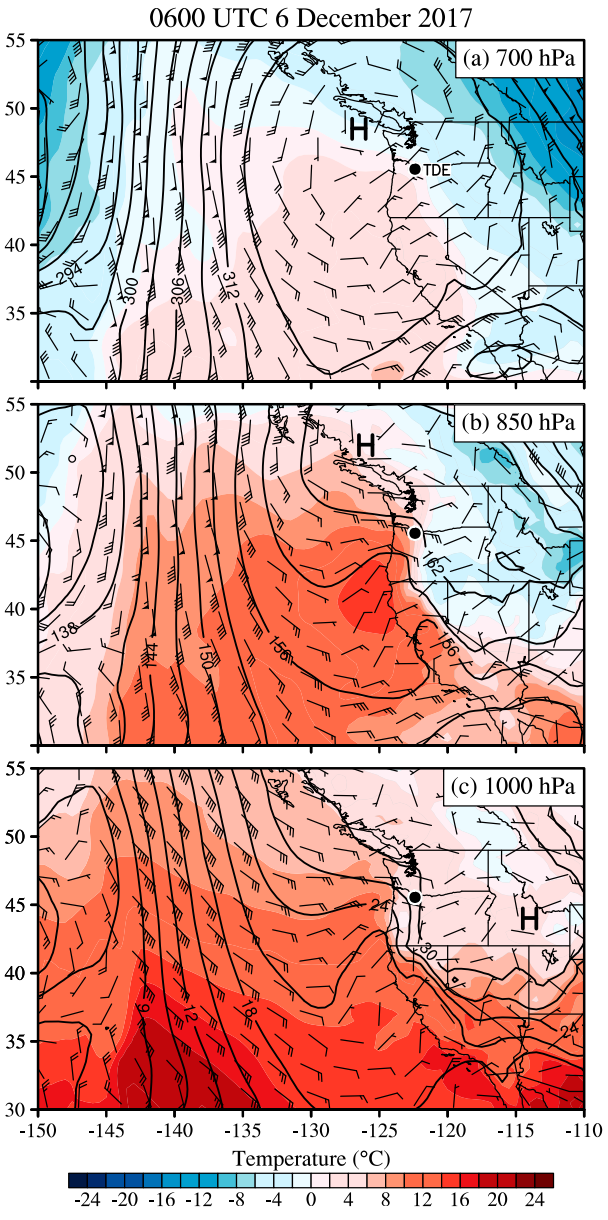

FIG. 5. As in Fig. 3, but for 0600 UTC 6 Dec 2017. The anticyclone center is marked with an "H."

high-frequency noise. Then, each smoothed vertical profile is individually normalized as a percentage of the strongest easterly flow within that profile. This normalization procedure—which yields the variable called the normalized u comp—is implemented to utilize constant-value thresholding, from one profile to the next, later in the analysis. An example of these results is shown in Fig. 7b for the same period as in Fig. 6. The normalized u-comp minima in each smoothed profile are identified using a vertically sliding three-point technique, where the centered normalized u-comp value of the triplet must be less than both neighboring values. A special boundary condition defines a local minimum at the first (last) radar range gate when the normalized u comp of the neighboring gate above (below) is greater than that at the boundary. It is also assumed that the normalized u-comp minimum associated with gap flow must be at least 30% of the strongest normalized u comp in the profile. The detection of normalized u-comp minima is illustrated in the example hourly profile at 0630 UTC 6 December extracted from Fig. 7b and shown in Fig. 8. Using the aforementioned criteria, four normalized u-comp minima are identified and depicted with circles in the normalized u-comp profile highlighted in these two figures.

The second step identifies the wind shear maxima above each of the previously identified normalized u-comp minima. Above the normalized u-comp minima associated with the gap flow, we define and seek to identify the height associated with the wind shear maxima as the top of the gap flow (i.e., the gap-flow depth). The wind shear is represented as the sum of the vertical gradients of nine-point smoothed u comp and v comp (not shown), where these gradients are calculated using a centered finite difference. This wind shear proxy captures flow regimes where either veering or backing winds exist above the gap flow, or where the wind speed decreases above the gap flow during unidirectional flow regimes. The same nine-point smoother described above is then applied to the time–height section of vertical shear (not shown). The individual vertical profiles in this time–height section are then normalized as a percentage of the maximum absolute value within each of those profiles (i.e., normalized uv-comp vertical shear). The normalized uv-comp vertical shear is shown in Fig. 7c.

The local maxima in normalized uv-comp vertical shear are identified in each vertical layer that is bounded by the heights of each adjacent pair of the normalized u-comp minima using the same three-point technique previously described, and are depicted with six circles in the example profile in Figs. 7c and 8. The unbounded vertical layer below the lowest (above the highest) normalized u-comp minimum is constrained by the height of the first (last) radar range gate or by a 0.75 km offset below (above) the height of the bounded u-comp minimum, whichever condition occurs first. In addition, when multiple local shear maxima exist in a layer, they are all identified and later assessed as gap-flow-depth candidates. For example, two maxima in normalized uv-comp vertical shear (i.e., labels 3a and 3b in Fig. 8) exist in the layer bounded by the normalized u-comp minima at 1.25 km MSL (i.e., label 3 in Fig. 8) and 2.0 km MSL (i.e., label 4 in Fig. 8). Last, in an effort to reduce the influence of noisy radar signals at higher ranges

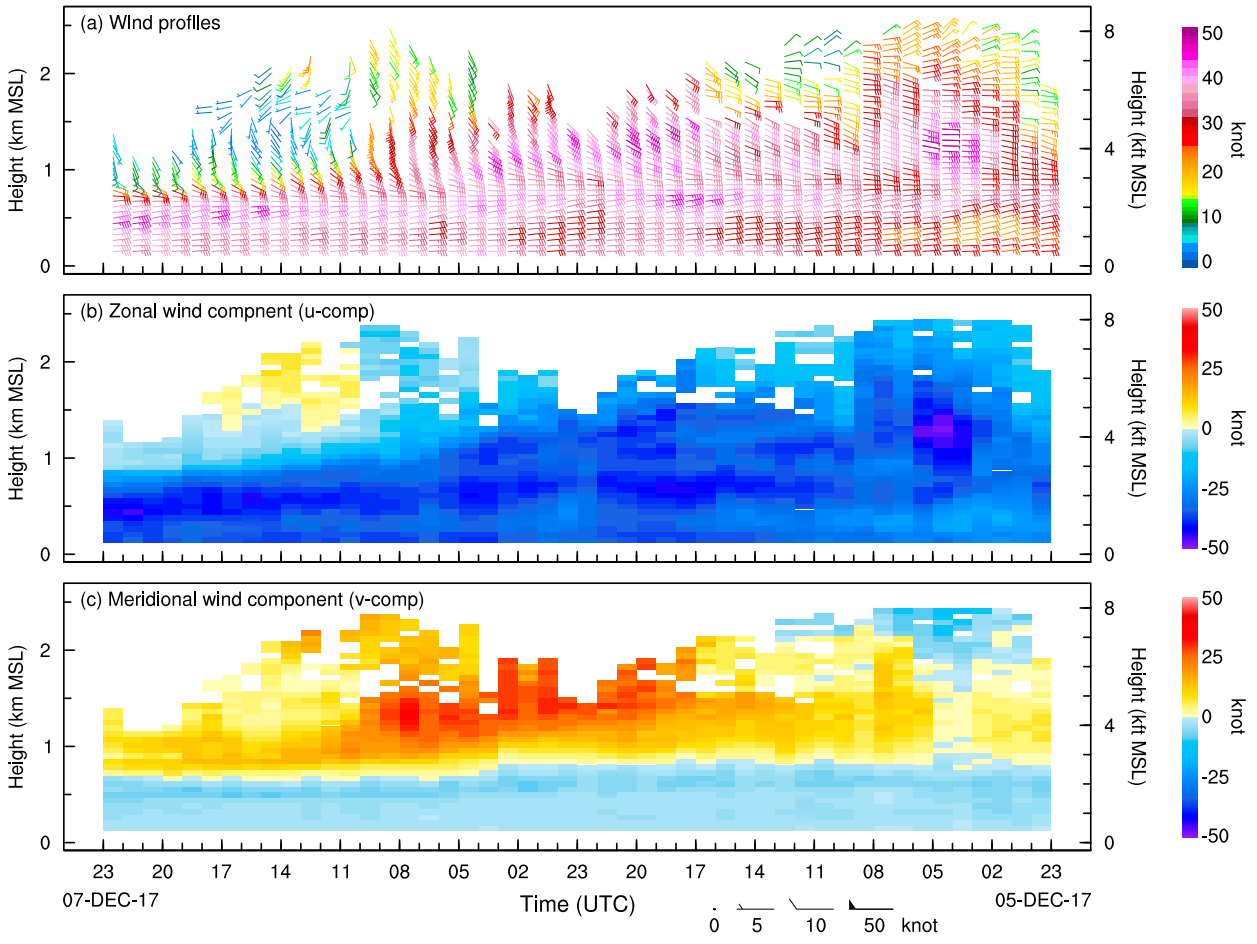

FIG. 6. Time–height sections of color-coded hourly data from the TDE wind profiler between 2300 UTC 5 Dec and 2300 UTC 7 Dec 2017: (a) wind profiles, as in Fig. 4a; (b) zonal wind component (i.e., *u* comp; kt), where easterly flow is less than 0 kt; and (c) meridional wind component (i.e., *v* comp; kt), where southerly flow is greater than 0 kt.

(i.e., in weak backscatter regions), normalized *uv*-comp vertical shear maxima above 1.5 km MSL must have shear values within 40% of the maxima in at least two of the six neighboring radar gates centered about the maxima. For normalized *uv*-comp vertical shear maxima that fail this test, accompanying normalized *u*-comp minima are not considered. For example, the two local shear maxima at ~2.05 and ~2.2 km MSL (i.e., labels 4a and 4b in Fig. 8) only have a single neighboring gate with shear values within 40% of their respective maxima; these maxima and the normalized *u*-comp minimum at ~2.0 km MSL (i.e., label 4 in Fig. 8) are therefore excluded from the analysis.

The third step analyzes all of the previously identified maxima in normalized *uv*-comp vertical shear (i.e., the gap-flow-depth candidates) and selects the one that best represents the gap-flow depth. This begins by identifying the three gap-flow-depth candidates with the largest normalized vertical-shear values. Next, for each of these three candidates, the vertical rate of change of the normalized *uv*-comp vertical shear below the shear maximum is calculated. Here, the greatest rate of change between the shear maximum and any two contiguous-gate-shear average within the six-gate layer below the maxima is used. Given the propensity for the vertical shear to decrease rapidly above gap flows, the final gap-flow-depth candidate with the greatest rate of change in normalized vertical shear is selected. Based on the criteria described above, label 2 on the normalized shear curve in Fig. 8 is tagged as the gap-flow depth. In addition, it is readily apparent that label 2 on the companion normalized *u*-comp curve is the gap-flow jet.

The fourth step takes into consideration the temporal behavior of the gap-flow depth. Once the first three steps are completed for all profiles in the 48-h period, temporal smoothing is applied to the time series of hourly gap-flow depth using a 1–2–1 weighted running average over the same 48-h period. Temporal interpolation is

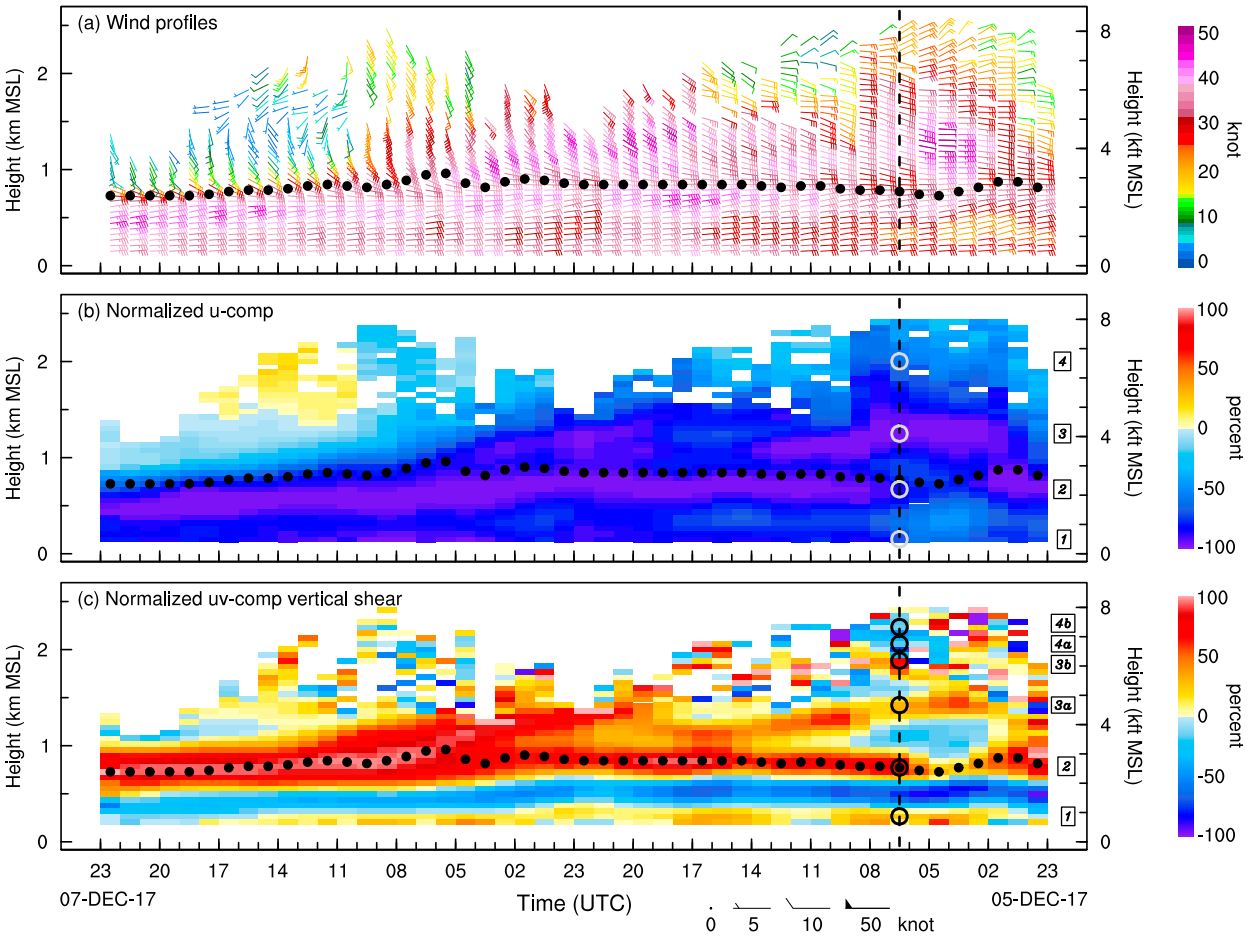

FIG. 7. Time–height sections of color-coded hourly data from the TDE wind profiler between 2300 UTC 5 Dec and 2300 UTC 7 Dec 2017: (a) wind profiles, as in Fig. 4a; (b) normalized *u*-comp (%); and (c) normalized *uv*-comp vertical shear (%). The solid black dots denote the top of the gap flow, as in Figs. 4a–c. The vertical black dashed line at 0630 UTC 6 Dec 2017 marks the center time of the hourly wind profile shown in Fig. 8. The open light-gray circles labeled 1, 2, 3, and 4 in (b) correspond to the local minima in normalized *u* comp (i.e., the strongest easterly flow) for the profile at 0630 UTC 6 Dec. The open black circles labeled 1, 2, 3a, 3b, 4a, and 4b in (c) correspond to local maxima in normalized *uv*-comp vertical shear for the same profile and are the candidate heights used for determining the top of the gap flow for that profile.

then applied to the smoothed time series when missing gap-flow-depth periods up to 3 h in duration are temporally bounded by valid gap-flow depths. To ensure continuity, the interpolation is only carried out when the bordering gap-flow depths are within 1 km of each other and have wind directions between 0° and 180° in the closest of the three lowest gates.

The fifth and final step removes gap-flow-depth outliers from the temporally smoothed and interpolated time series. Low data-quality confidence is assumed when gap-flow depths are temporally isolated and are removed when either of the following two conditions exist: 1) a single hourly gap-flow depth is temporally bordered by missing hourly gap-flow depths, or 2) two consecutive hourly gap-flow depths are temporally bordered by two consecutively missing hourly gap-flow depths. An example of the finalized 48-h time–height gap-flow depth results are shown in Fig. 7, where the gap-flow depth is depicted with bold black dots.

Despite the previously described efforts to improve data quality, erroneous results still occurred on rare occasions. These errors were in the form of false alarms, inaccurate height representations, and detection failure. To assess these errors, gap-flow-depth results spanning two cold seasons (October–April of 2015/16 and 2016/17) at TDE were visually inspected and validated using time–height cross sections of radar winds and subjective meteorological reasoning. False-alarm depths (i.e., times when a depth value was produced without temporally coherent gap-flow conditions present) occurred 0.13% (5 of 3926)

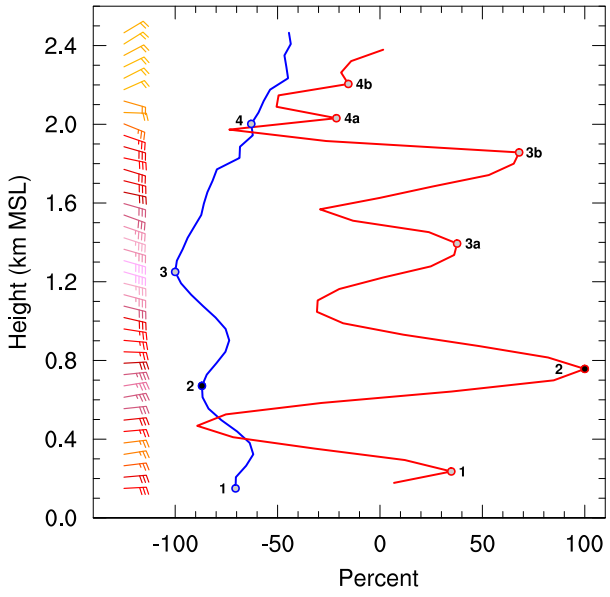

FIG. 8. Hourly wind profile from the TDE wind profiler, time centered at 0630 UTC 6 Dec 2017. Color-coded wind barbs are as in Fig. 4a. The blue and red profiles are the normalized *u*-comp and the normalized *uv*-comp vertical shear, respectively (%). The dots labeled on the blue and red profiles are the same as those shown and described in Figs. 7b and 7c, respectively. The black-filled dots labeled "2" mark the primary gap-flow jet on the blue profile and the top of the gap flow on the red profile.

of the time. During times of gap flow, 1.48% (58 of 3926) of the depth values were associated with a height-representation error of 100–600 m. These errors occurred with deep easterly flow regimes, shallow gap flows near or below the first two radar range gates (<0.2 km), complex vertical wind shear structure above the gap-flow jet, and either poor-quality or missing wind data. The times when the algorithm failed to detect gap-flow depths during gap-flow conditions were almost exclusively associated with shallow gap flows, when the gap-flow jet and its overlying vertical wind shear were inadequately resolved near the minimum range of the radar.

b. *Precipitation typing*

The details of our automated precipitation type (*p* type) processing, which ultimately identifies rain, freezing rain, and snow, begins with utilizing surface-based disdrometer measurements to identify falling rain and snow via the methodology of Yuter et al. (2006). Specifically, each disdrometer-detected hydrometeor is assigned as a rain or not-rain classification using empirically based hydrometeor velocity–diameter relationships, where not-rain is any precipitation that is not classified as rain. Within each 2-min observing interval, our *p*-type processing calculates a rain fraction, defined as the ratio of rain counts to the sum of both rain and not-rain counts collected over the period. To determine the *p* type during each 2-min period, we need to define a logical rain-fraction threshold to distinguish between rain and snow. This threshold is derived hereafter by calibrating the disdrometer rain fractions against independently observed precipitation typing from a nearby location.

The proximity of the disdrometer at TDE to the NWS observing stations at the collocated Troutdale airport and at nearby PDX between 22 November 2016 and 30 June 2017 provides a unique opportunity to compare the disdrometer rain fractions with the present weather reports in the NWS METAR observations. During this period, the present weather reports were deemed more complete and more reliable at PDX, hence we used those reports. In Fig. 9, scatterplots of disdrometer rain fraction versus collocated surface wind speed are stratified by METAR *p* type and reveal that most of the METAR snow (rain/freezing rain) reports correspond to small (large) disdrometer rain fractions. However, primarily for rain and freezing rain, there appear to be disdrometer rain-fraction misrepresentations. Most prevalently, in the METAR rain-only panel (Fig. 9a), there is a clustering of data points that extend from large to small rain fractions at wind speeds $>\sim 6\,\mathrm{m\,s^{-1}}$, some of which overlap with the small rain fractions associated with the METAR snow-only population (Fig. 9b). This seemingly wind-affected characteristic exists, but to a lesser extent, within the METAR freezing-rain sample (Fig. 9c). Strong winds were, in fact, shown to adversely impact the quality of disdrometer measurements and interpretations in an earlier study by Friedrich et al. (2013). Data quality also appears to be compromised at both zero rain fraction and zero wind speed. The suspicious data points at zero rain fraction are likely related to unknown instrument issues and are therefore excluded from the subsequent analysis, whereas most of the data points at zero wind speed likely result from a frozen anemometer.

The disdrometer rain-fraction distributions in Fig. 9 are used to initially assign automated disdrometer *p* types. Visual inspection of the nonzero rain fractions reveals a large majority of the METAR-observed snowfall (i.e., 94%) occurring with rain fractions less than 0.35 and a majority of the METAR-observed rain (i.e., 94%) and freezing rain (i.e., 97%) occurring with rain fractions greater than 0.35. We therefore use 0.35 as a starting-point threshold for discriminating between snow versus rain and freezing rain.

Independent meteorological measurements at TDE are utilized to address disdrometer quality-control

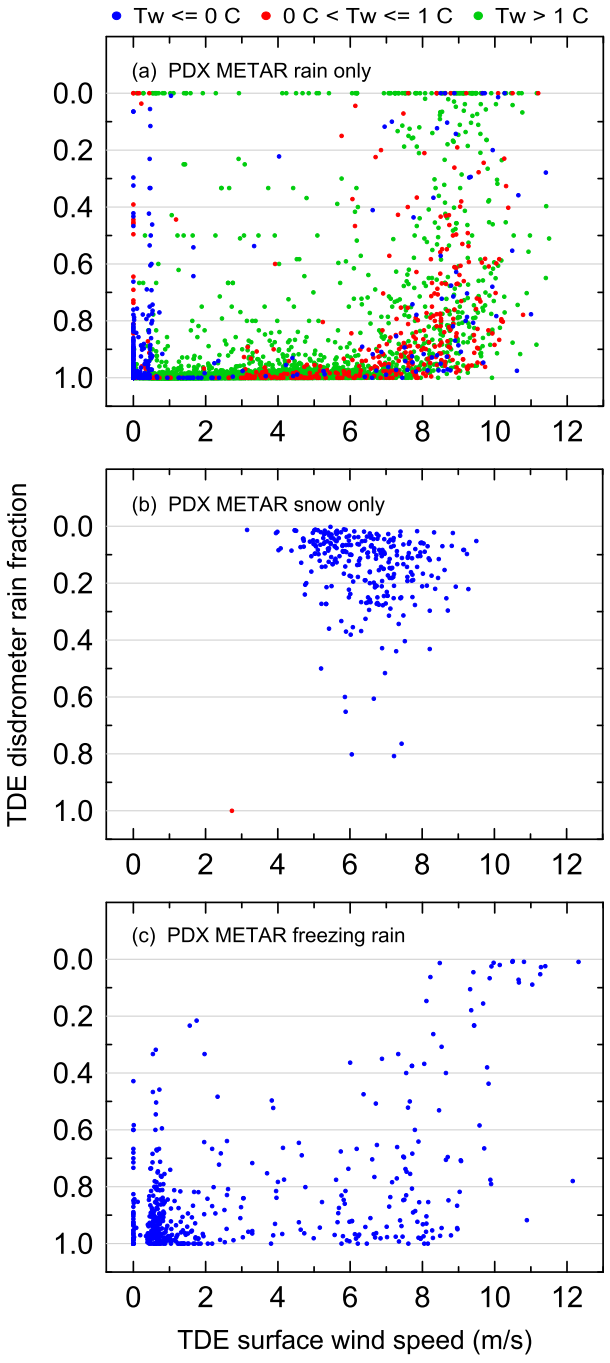

FIG. 9. PARSIVEL rain fraction as a function of surface wind speed at TDE, stratified by the observed METAR precipitation type at PDX: (a) PDX rain, (b) PDX snow, and (c) PDX freezing rain. All samples are color coded by surface T_w (°C). The lone red dot in the bottom left of (b) represents a data point with $T_w = 1.56$°C.

issues associated with precipitation type and strong wind. Measurements from the vertically oriented beam of a collocated radar wind profiler, a heated tipping-bucket rain gauge, 2-m temperature and humidity sensors, and a 10-m anemometer reveal the following:

1) Surface $T_w > 1$°C is associated exclusively with METAR rain observations (see color-coded T_w in Fig. 9).
2) In Fig. 10a, and, to a lesser extent in Fig. 10c, a large proportion of the discrepancies between the METAR and disdrometer p type during strong winds are associated with radar-measured hydrometeor fall velocities in the vertical beam $R_v \geq 3\,\mathrm{m\,s^{-1}}$. Values of R_v greater than or equal to this magnitude are predominantly associated with rain (Ralph et al. 1995). And as reinforced by Fig. 10b, there are no samples in the snow population with $R_v \geq 3\,\mathrm{m\,s^{-1}}$.
3) As verified by both the radar and tipping bucket, disdrometer-inferred hydrometeors are falsely reported during windy, precipitation-free periods, which suggests that there may be a vibrational component to the contaminated disdrometer measurements during both precipitating and nonprecipitating conditions (not shown).
4) During periods of snow, the tipping bucket often fails to detect measureable precipitation, as revealed in Figs. 2b and 2e. The tipping bucket also occasionally fails to detect measureable light rain and drizzle (not shown).

These independent meteorological measurement findings are used to confirm or reassign disdrometer p-type identifications based on heuristic meteorological reasoning. The surface T_w, which is closest in time and within ±2 min of each 2-min disdrometer sample, is used to reassign those disdrometer snow-sample identifications to rain for $T_w > 1$°C, since it is uncommon to observe snow in conditions warmer than this threshold [as Fig. 9b highlights, and as Lundquist et al. (2008) demonstrated for the windward slope of California's Sierra Nevada (they used actual air temperature, which should not be much warmer than the wet-bulb in the presumably near-saturated conditions during accumulating precipitation)]. Also, the lowest two-gate average of R_v is used to reassign disdrometer snow-sample identifications to rain when the average R_v exceeds $3\,\mathrm{m\,s^{-1}}$. Here, the lowest two gates are vertically centered at 0.15 and 0.21 (0.16 and 0.27) km MSL in the 60 (105)-m mode, respectively, and R_v is used from the mode that is within ±2 min of each disdrometer sample. Finally, the surface temperature closest in time is used to reassign the remaining rain samples to freezing rain for all values at or below freezing.

Since the disdrometer falsely reports precipitation during windy periods, each 2-min sample only includes a disdrometer p-type identification when precipitation is concurrently detected by either the tipping bucket or the radar within ±2 min of the disdrometer sample.

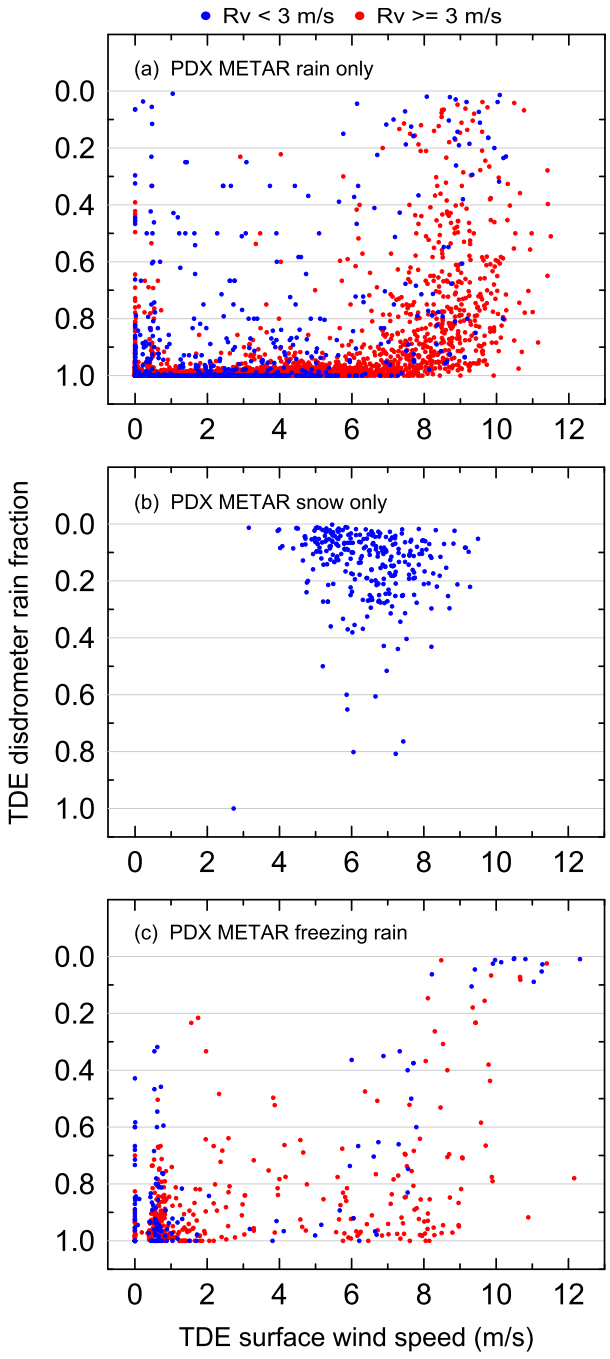

FIG. 10. PARSIVEL rain fraction as a function of surface wind speed at TDE, stratified by the observed METAR precipitation type at PDX: (a) PDX rain, (b) PDX snow, and (c) PDX freezing rain. All samples are color coded by the lowest two-gate average of R_v (m s^{-1}).

Utilization of the radar is necessary for identification of snow or light rain/drizzle, when catchment or sensitivity limitations of the tipping-bucket measurement occur. The precipitation-identification criteria for the tipping bucket is a single tip (0.254 mm) and, for the radar, the lowest-two-gate-average of reflectivity factor and R_v must be greater than or equal to 20 dBZ and 0.5 m s^{-1}, respectively. These reflectivity-factor and R_v thresholds also advantageously prevent ground-clutter contamination of the radar precipitation identification, since ground-clutter signals are characterized by reflectivity values generally less than 20 dBZ in combination with vertical radial velocities near 0 m s^{-1}.

Last, a special condition is implemented for precipitation identification using the tipping bucket alone, since single-tip measurements (0.254 mm) can temporally lag the actual time of precipitation owing to instrument response/sensitivity constraints. To account for this, the temporal matching window between the 2-min tipping-bucket and disdrometer samples is expanded to +60 min for 1-h periods with a single-tip occurrence.

The application of the aforementioned methodology yields the results in Fig. 11, which are color coded by the automated disdrometer p type of rain, snow, and freezing rain. In the METAR-observed rain conditions (Fig. 11a), a large majority of the disrometer rain fractions greater than 0.35 are p typed as rain at TDE (96%) and the remainder are p typed as freezing rain (4%). It is plausible that many of these freezing rain samples are not erroneous but rather are the result of real differences in p type between TDE and PDX. PDX is located 15 km downriver from TDE and, therefore, farther from the colder continental cold-air source flowing out of the gorge. Hence, there can be times when rain is freezing on contact at TDE but not at PDX. For the few remaining rain-fraction points less than 0.35, p types not identified as rain are most likely misrepresented by the automated methodology, comprising 1% of the total METAR rain population. In the METAR-observed snow (Fig. 11b), all of the disdrometer rain fractions less than 0.35 are accurately identified as snow using the automated methodology. There are a few remaining points greater than 0.35, which are likely miscategorized as rain and freezing rain, and represent 6% of the total METAR snow population. Finally, in the METAR-observed freezing rain (Fig. 11c), all disdrometer rain fractions greater than 0.35 are accurately identified as freezing rain using the automated methodology. For rain fractions less than 0.35, a small number of points (3% of the total METAR freezing-rain population) are either miscategorized as snow or the result of real differences in p type between TDE and PDX.

All of the preceding, potentially miscategorized, 2-min automated disdrometer p types are implicitly filtered by identifying the most frequently occurring 2-min p type over a longer time period. A 1-h period is chosen, which also matches the 1-h resolution of the wind

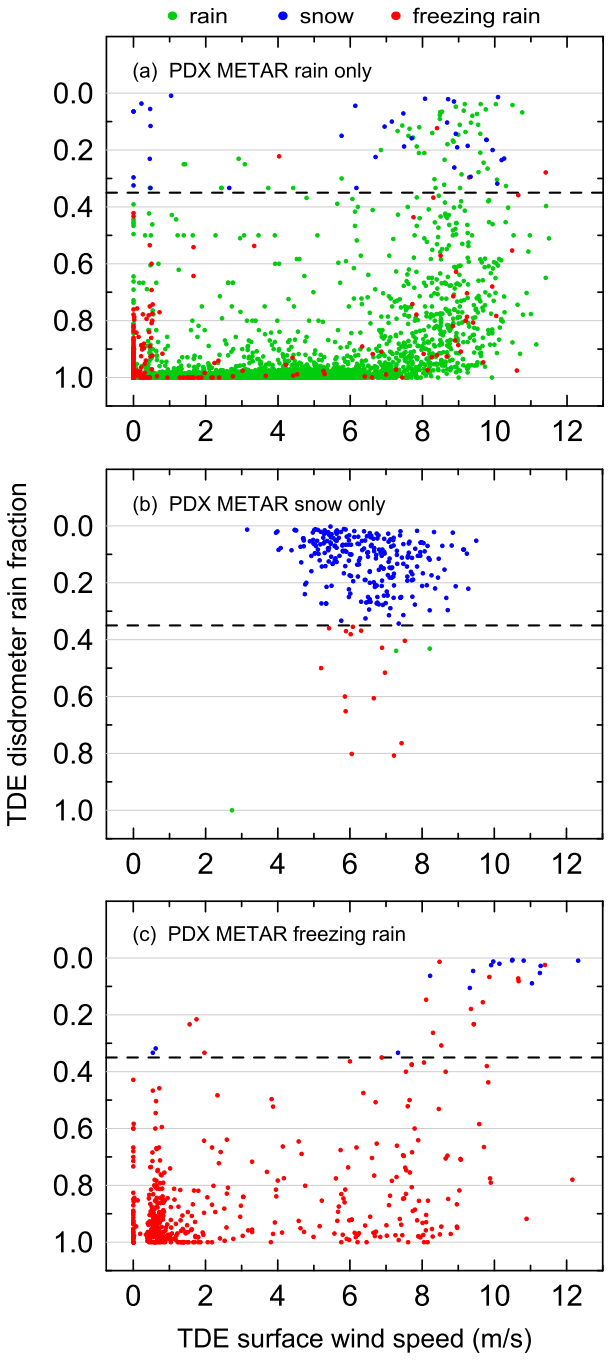

FIG. 11. PARSIVEL rain fraction as a function of surface wind speed at TDE, stratified by the observed METAR precipitation type at PDX: (a) PDX rain, (b) PDX snow, and (c) PDX freezing rain. All samples are color coded by the automated disdrometer p type. Rain fractions equal to 0 are excluded. The horizontal dashed line at rain fraction = 0.35 in each panel represents the threshold that distinguishes between snow (<0.35) and rain/freezing rain (≥ 0.35).

profiles. Hourly dominant disdrometer p types derived solely from radar-identified precipitation must occur over at least five (ten) ~30-s-averaged vertical-beam observations per each hour for snow (rain), where the larger radar-observation count for rain is used to help filter out high-frequency signals during short-lived convection. Based on the automated disdrometer-based p-type results in Fig. 11 and the subsequent partitioning of these results into 1-h blocks, the rain-fraction threshold of 0.35 does indeed appear to automatically differentiate between snow versus rain and freezing rain in reliable fashion.

5. Conclusions

Measurements from multiple remote sensing and in situ instruments at Troutdale, Oregon, have been combined into a real-time, hourly updating, online data product that highlights atmospheric conditions associated with shallow, westward-directed gap-flow events exiting the Columbia River Gorge and precipitation-related hazards such as snow, freezing rain, and heavy rain. This product also graphically establishes a connection between shallow, cold gap-flow events in winter and the occurrence of freezing rain and/or snow in the normally maritime environment present in the metropolitan area encompassing Portland, Oregon, and Vancouver, Washington.

The development of this data product was motivated by an operational forecasting challenge specific to the Portland WFO and the Columbia River Gorge. Its application to the forecasting process is twofold. First, having all of the relevant gap-flow-related observations collectively depicted in a single graphic improves forecaster situational awareness for identifying warning-level criteria to help ensure public safety in the densely populated Portland–Vancouver metropolitan area. For example, the depth of the cold gap flow, as measured by the wind profiler and RASS, combined with the p-type information can be used to assess the present and near-term frozen-precipitation risk, and the strength of the observed flow can be used to verify or infer the risk for potentially damaging winds downstream of the gap. Second, forecasters can use the spatiotemporal characteristics of the collective observations to qualitatively assess forecast-model confidence and make modifications to the public forecast based on biases or discrepancies that the observations reveal in the recently verified model forecast.

The data product also provides additional research opportunities to improve model forecasts of gap-flow phenomena, such as those from the NOAA High Resolution Rapid Refresh model (HRRR). The fine spatiotemporal resolution of the observations, combined

with the newly developed gap-flow-depth metric, can be used to assess high-resolution model performance. In addition to quantifying forecast bias, this performance evaluation could identify recurring model deficiencies and potentially isolate the most prominent physical processes associated with those deficiencies. For example, the cessation of easterly gap-flow events (and their associated wind and precipitation hazards), which often pose forecasting challenges for the models, frequently coincide with landfalling midlatitude synoptic cyclones. During these times, as the gap flow accelerates in response to a strengthening east–west-oriented pressure gradient (i.e., decreasing pressure along the coast associated with the approaching cyclone coupled with high pressure inland associated with a preexisting cold continental air mass), the gap-flow depth typically decreases with time. One plausible mechanism for this depth decrease (and the eventual termination of easterly gap flow) is the role of turbulent mixing in an environment of increased vertical shear and/or decreased thermodynamic stability. A bulk-stability analysis could be conducted using wind profiler and RASS data to test this hypothesis, which, upon verification, could lead to more focused modeling studies into the sensitivity of turbulence parameterizations on the evolution of gap-flow depth.

This real-time, web-based data product can be accessed on an interactive web page (http://www.esrl.noaa.gov/psd/data/obs/datadisplay/) by scrolling down the station list on the right side of the web page to ''Troutdale (tde)'' and then clicking on ''Precipitation Hazard Plot'' link. This product has already been deemed extremely useful for situational awareness at the NWS PDX forecast office. If this online product evolves into an important component of the forecast and warning-decision process, additional development can be pursued to visualize the product in the Advanced Weather Interactive Processing System (AWIPS2) to make it more convenient for forecasters to access. Last, a similar data product could also be applied to terrain gaps in other geographical regions assuming the parties of interest could either purchase or rent the various types of observing equipment used in this study, all of which are commercially available. Even for the Columbia Gorge highlighted in this study, it is plausible to utilize the data product at a site east of the gap to monitor and study eastward-directed gap flows, which frequently occur and are often accompanied by low-level jet structures during the warm season.

Acknowledgments. The authors wish to thank the talented engineering crew at NOAA/ESRL/PSD for installing and maintaining the observing equipment at Troutdale, Oregon. We also appreciate input from Dr. David Kingsmill regarding interpretation of PARSIVEL disdrometer datasets. We are grateful for comments offered by three anonymous reviewers. Their input improved the scope and quality of this manuscript. This work was supported by NOAA's Atmospheric Science for Renewable Energy Program and by the U.S. Department of Energy's Office of Energy Efficiency and Renewable Energy under Interagency Agreement DE-EE0007605. Opinions represented in this article are the authors' own and do not necessarily reflect the view of the DOE or the U.S. government.

REFERENCES

Bond, N. A., and Coauthors, 1997: The Coastal Observation and Simulation with Topography (COAST) experiment. *Bull. Amer. Meteor. Soc.*, **78**, 1941–1955, https://doi.org/10.1175/1520-0477(1997)078<1941:TCOASW>2.0.CO;2.

Carter, D. A., K. S. Gage, W. L. Ecklund, W. M. Angevine, P. E. Johnston, A. C. Riddle, J. S. Wilson, and C. R. Williams, 1995: Developments in UHF lower tropospheric wind profiling at NOAA's Aeronomy Laboratory. *Radio Sci.*, **30**, 977–1001, https://doi.org/10.1029/95RS00649.

Colle, B. A., K. A. Loescher, G. S. Young, and N. S. Winstead, 2006: Climatology of barrier jets along the Alaskan coast. Part II: Large-scale and sounding composites. *Mon. Wea. Rev.*, **134**, 454–477, https://doi.org/10.1175/MWR3038.1.

Colman, B. R., and C. F. Dierking, 1992: The Taku wind of southeast Alaska: Its identification and prediction. *Wea. Forecasting*, **7**, 49–64, https://doi.org/10.1175/1520-0434(1992)007<0049:TTWOSA>2.0.CO;2.

Friedrich, K., S. Higgins, F. J. Masters, and C. R. Lopez, 2013: Articulating and stationary PARSIVEL disdrometer measurements in conditions with strong winds and heavy rainfall. *J. Atmos. Oceanic Technol.*, **30**, 2063–2080, https://doi.org/10.1175/JTECH-D-12-00254.1.

Glickman, T., Ed., 2000: *Glossary of Meteorology*. 2nd ed. Amer. Meteor. Soc., 855 pp., http://glossary.ametsoc.org/.

Löffler-Mang, M., and J. Joss, 2000: An optical disdrometer for measuring size and velocity of hydrometeors. *J. Atmos. Oceanic Technol.*, **17**, 130–139, https://doi.org/10.1175/1520-0426(2000)017<0130:AODFMS>2.0.CO;2.

Loescher, K. A., G. S. Young, B. A. Colle, and N. S. Winstead, 2006: Climatology of barrier jets along the Alaskan coast. Part I: Spatial and temporal distributions. *Mon. Wea. Rev.*, **134**, 437–453, https://doi.org/10.1175/MWR3037.1.

Lundquist, J. D., P. J. Neiman, B. E. Martner, A. B. White, D. J. Gottas, and F. M. Ralph, 2008: Rain versus snow in the Sierra Nevada, California: Comparing Doppler profiling radar and surface observations of melting level. *J. Hydrometeor.*, **9**, 194–211, https://doi.org/10.1175/2007JHM853.1.

Martner, B. E., and Coauthors, 1993: An evaluation of wind profiler, RASS, and microwave radiometer performance. *Bull. Amer. Meteor. Soc.*, **74**, 599–613, https://doi.org/10.1175/1520-0477(1993)074<0599:AEOWPR>2.0.CO;2.

Neiman, P. J., F. M. Ralph, A. B. White, D. D. Parrish, J. S. Holloway, and D. L. Bartels, 2006: A multiwinter analysis of channeled flow through a prominent gap along the northern California coast during CALJET and PACJET. *Mon. Wea. Rev.*, **134**, 1815–1841, https://doi.org/10.1175/MWR3148.1.

Overland, J. E., and B. A. Walter, 1981: Gap winds in the Strait of Juan de Fuca. *Mon. Wea. Rev.*, **109**, 2221–2233, https://doi.org/10.1175/1520-0493(1981)109<2221:GWITSO>2.0.CO;2.

Ralph, F. M., P. J. Neiman, D. W. van de Kamp, and D. C. Law, 1995: Using spectral moment data from NOAA's 404-MHz radar wind profilers to observe precipitation. *Bull. Amer. Meteor. Soc.*, **76**, 1717–1739, https://doi.org/10.1175/1520-0477(1995)076<1717:USMDFN>2.0.CO;2.

Sharp, J. M., and C. F. Mass, 2002: Columbia Gorge gap flow: Insights from observational analysis and ultra-high-resolution simulation. *Bull. Amer. Meteor. Soc.*, **83**, 1757–1762, https://doi.org/10.1175/BAMS-83-12-1757.

——, and ——, 2004: Columbia Gorge gap winds: Their climatological influence and synoptic evolution. *Wea. Forecasting*, **19**, 970–992, https://doi.org/10.1175/826.1.

Steenburgh, W. J., C. F. Mass, and S. A. Ferguson, 1997: The influence of terrain-induced circulations on wintertime temperature and snow level in the Washington Cascades. *Wea. Forecasting*, **12**, 208–227, https://doi.org/10.1175/1520-0434(1997)012<0208:TIOTIC>2.0.CO;2.

Stewart, R. E., J. D. Marwitz, J. C. Pace, and R. E. Carbone, 1984: Characteristics through the melting layer of stratiform clouds. *J. Atmos. Sci.*, **41**, 3227–3237, https://doi.org/10.1175/1520-0469(1984)041<3227:CTTMLO>2.0.CO;2.

Weber, B. L., D. B. Wuertz, D. C. Welsh, and R. McPeek, 1993: Quality controls for profiler measurements of winds and RASS temperatures. *J. Atmos. Oceanic Technol.*, **10**, 452–464, https://doi.org/10.1175/1520-0426(1993)010<0452:QCFPMO>2.0.CO;2.

White, A. B., D. J. Gottas, E. Strem, F. M. Ralph, and P. J. Neiman, 2002: An automated bright-band height detection algorithm for use with Doppler radar vertical spectral moments. *J. Atmos. Oceanic Technol.*, **19**, 687–697, https://doi.org/10.1175/1520-0426(2002)019<0687:AABHDA>2.0.CO;2.

——, ——, A. F. Henkel, P. J. Neiman, F. M. Ralph, and S. I. Gutman, 2010: Developing a performance measure for snow-level forecasts. *J. Hydrometeor.*, **11**, 739–753, https://doi.org/10.1175/2009JHM1181.1.

Williams, C. R., K. S. Gage, W. Clark, and P. Kucera, 2005: Monitoring the reflectivity calibration of a scanning radar using a profiler radar and a disdrometer. *J. Atmos. Oceanic Technol.*, **22**, 1004–1018, https://doi.org/10.1175/JTECH1759.1.

Yuter, S. E., D. E. Kingsmill, L. B. Nance, and M. Löffler-Mang, 2006: Observations of precipitation size and fall speed characteristics within coexisting rain and wet snow. *J. Appl. Meteor.*, **45**, 1450–1464, https://doi.org/10.1175/JAM2406.1.